https://doi.org/10.5194/egusphere-2026-1809
Preprint. Discussion started: 16 April 2026

Kilometer-scale distributed temperature sensing reveals heterogeneous permafrost warming near Arctic infrastructure

Xiaohang Ji,[1] Eileen R. Martin[2], Ming Xiao[3], Ahmad Tourei[4], Dmitry Nicolsky[5], Anne Jensen[6]

[1] Graduate Student, Department of Civil and Environmental Engineering, The Pennsylvania State University, University Park, PA 16802, U.S.A. Email: jixiaohang2014@gmail.com.
[2] Associate Professor, Department of Geophysics, Department of Applied Math and Statistics, and Hydrologic Science and Engineering Program, Colorado School of Mines, Golden, CO 80401, U.S.A. Email: eileenrmartin@mines.edu.
[3] Professor, Department of Civil and Environmental Engineering, The Pennsylvania State University, University Park, PA 16802, U.S.A. Email: mzx102@psu.edu. Corresponding author.
[4] Graduate Student, Hydrologic Science and Engineering Program, Colorado School of Mines, Golden, CO 80401, U.S.A. Email: tourei@mines.edu.
[5] Assistent Professor, Geophysical Institute, University of Alaska Fairbanks, Fairbanks, AK, USA. Email: djnicolsky@alaska.edu.
[6] Affiliate Faculty, Department of Anthropology, University of Alaska Fairbanks, Fairbanks, AK, USA. Email: ajensen@alaska.edu.

Correspondence to: Ming Xiao, mzx102@psu.edu

Abstract

Accelerated Arctic warming is destabilizing permafrost, threatening ecosystems, infrastructure, and northern communities, yet permafrost thermal dynamics remain poorly characterized and highly uncertain due to sparse observations and limited representation of fine-scale heterogeneity. Here we combine kilometer-scale distributed temperature sensing (DTS) with data-driven hysteresis modeling to resolve spatiotemporal variability in permafrost temperatures across disturbed and undisturbed Arctic landscapes near Utqiaġvik, Alaska. A 2-km fiber-optic array recorded continuous ground temperatures from 2021 to 2024, revealing persistent warming associated with civil infrastructure and pronounced thermal heterogeneity in patterned tundra. Ice-wedge polygon troughs consistently exhibit lower temperatures than polygon centers, highlighting the role of subsurface ice distribution in controlling ground thermal regimes. Using these observations, we develop a multivariate hysteresis model that captures lagged ground–air temperature responses and incorporates snow, precipitation, wind, atmospheric pressure, and ground surface conditions. The model accurately reproduces observed permafrost temperatures, fills observational gaps, and enables projections under future climate scenarios. Projections indicate continued warming through 2075, with enhanced temperature increases in infrastructure areas and ice-rich terrains. Our results demonstrate the power of DTS to resolve permafrost thermal heterogeneity at unprecedented scales and provide a transferable framework for predicting permafrost temperature dynamics in a rapidly warming Arctic.

https://doi.org/10.5194/egusphere-2026-1809
Preprint. Discussion started: 16 April 2026

1. Introduction

Permafrost underlies approximately one quarter of the land area in the Northern Hemisphere and plays a critical role in regulating Arctic landscape stability, ecosystem function, and carbon storage (Jorgenson et al., 2010; Romanovsky et al., 2010; Geiger et al 2009). In the recent decades, accelerated Arctic warming has led to widespread permafrost warming and thawing, resulting in increased active-layer thickness, thermokarst development, and ground subsidence (Romanovsky et al., 2010; Farquharson et al., 2016). These changes increase the region's vulnerability to ground subsidence, coastal erosion, and infrastructure failure, with far-reaching consequences for ecosystems, greenhouse gas emissions, and the stability of northern infrastructure and communities (Jorgenson et al., 2010; Hjort et al. 2018).

Permafrost temperature is a key integrative indicator of subsurface thermal conditions and reflects the combined effects of atmospheric forcing, snow cover, soil thermal properties, moisture conditions, and geomorphology (Goodrich, 1982; Geiger et al., 2009; Nicolsky et al., 2009). However, permafrost thermal regimes are highly heterogeneous in space and time. Strong spatial variability occurs at scales ranging from meters to kilometers due to differences in vegetation, snow redistribution, soil composition, and geomorphology, particularly in landscapes characterized by ice-rich permafrost and patterned ground (Apaloo et al., 2012; Léger et al., 2019; Tourei et al. 2024). Temporally, permafrost temperatures exhibit pronounced seasonal variability associated with freeze–thaw processes and thermal inertia, resulting in delayed responses of ground temperature to changes in air temperature (Hasfurther and Burman, 1974; Hu et al., 2017).

Despite the importance of spatial and temporal variability, permafrost monitoring has traditionally relied on borehole-based point measurements. Borehole thermistors provide high-quality, long-term temperature records at discrete locations but are spatially sparse and insufficient for resolving fine-scale thermal heterogeneity across complex Arctic landscapes (Romanovsky et al., 2010; Harrington and Hayashi, 2019). As a result, critical thermal contrasts—such as those associated with ice-wedge polygons, infrastructure disturbance, and variable snow accumulation—are often underrepresented in observational datasets, limiting both process understanding and model evaluation (Farquharson et al., 2016).

Distributed Temperature Sensing (DTS) based on fiber-optic cables has emerged as a transformative tool for capturing high-resolution, continuous temperature profiles in permafrost regions (Ukil et al., 2011; Léger et al., 2019). DTS systems infer temperature from the backscattering of laser light along an optical fiber. Unlike conventional approaches, DTS provides spatially extensive data along fiber-optic cables and enables the detection of fine-scale thermal heterogeneity and long-term trends with detection accuracy of ±1 °C, spatial resolution in one meter or sub-meter scale, and measurement distance over a hundred km (Ukil et al., 2011; Harrington and Hayashi, 2019; Léger et al., 2019). DTS has been successfully applied in permafrost regions for various applications, including monitoring permafrost temperature along transportation infrastructure in Salluit, Nunavik (Roger et al., 2015), detecting gas migration in wellbores on the Alaska North Slope (Garcia-Ceballos et al., 2024), and observing permafrost degradation during controlled warming experiments in Fairbanks, Alaska (Wagner et al., 2018; Cheng et al., 2022). However, long-term DTS deployments spanning multiple years and diverse Arctic surface conditions is unprecedented, and their potential for advancing predictive understanding of permafrost thermal dynamics has not been fully explored.

https://doi.org/10.5194/egusphere-2026-1809
Preprint. Discussion started: 16 April 2026

Modeling permafrost temperature evolution commonly relies on physics-based heat-transfer models that explicitly represent soil thermal properties, phase change, snow insulation, and surface energy balance (Goodrich, 1982; Gao et al., 2003; Westermann et al., 2023). While these models have proven valuable for simulating permafrost processes, they require extensive parameterization and detailed input data that are often difficult to obtain in remote Arctic regions (Nicolsky et al., 2009; Jansson, 2012). Empirical approaches that relate ground temperature to air temperature offer a computationally efficient alternative, but they frequently struggle to capture delayed ground responses and seasonal asymmetry associated with freeze–thaw processes (Kang et al., 2000).

A defining feature of permafrost thermal behavior is hysteresis in the relationship between air temperature and ground temperature. Due to thermal inertia, latent heat effects, and moisture-dependent heat transfer, ground temperatures respond differently during warming and cooling phases, producing asymmetric freeze–thaw trajectories (Hu et al., 2017). Although hysteresis has been recognized in observational and modeling studies, it is often treated implicitly rather than incorporated explicitly into predictive frameworks that can leverage dense spatial observations (Lin et al., 2003).

In this study, we combine kilometer-scale distributed temperature sensing observations with a data-driven hysteresis modeling framework to characterize permafrost thermal dynamics across disturbed and undisturbed Arctic landscapes near Utqiaġvik, Alaska. A 2-km fiber-optic DTS array recorded continuous ground temperatures from 2021 to 2024 across civil infrastructure, non-patterned tundra, and ice-wedge polygon terrain. These observations reveal persistent infrastructure-related warming and pronounced thermal heterogeneity associated with patterned tundra. Patterned tundra exhibits surface-expressed ice-wedge polygonal microtopography, whereas non-patterned tundra lacks visible polygonal surface expression and appears laterally uniform at the ground surface (French 2017; Washburn 1956). Building on these data, we develop a multivariate hysteresis model that explicitly captures lagged ground–air temperature responses while accounting for key meteorological drivers and surface conditions. The model reproduces observed permafrost temperatures, fills observational gaps, and enables projections of future ground temperatures under climate-change scenarios both along the DTS transect.

2. Study area and DTS deployment

The study site is located near Utqiaġvik, Alaska in Arctic Coastal Plain within ice-rich tundra underlain by continuous permafrost (Fig. 1a). The region is characterized by ice-wedge polygon microtopography and has experienced rapid warming over recent decades (Wendler et al. 2014). Civil infrastructure within the study area includes buildings, roads, and buried utilities constructed directly on permafrost, providing an opportunity to examine anthropogenic impacts on ground thermal regimes. A 2-km fiber-optic flat-pack multimode DTS cable was deployed along a transect crossing civil infrastructure, undisturbed non-patterned tundra, and patterned tundra (Fig. 1c). The cable started from the Department of Energy (DOE) Atmospheric Radiation Measurement (ARM) facility, followed the service road of the National Oceanic and Atmospheric Administration (NOAA) facility, went under the crawl space of the new NOAA building, and extended into the tundra in the northeast direction toward Elson Lagoon (Fig. 1d). The fiber optic cable is connected

https://doi.org/10.5194/egusphere-2026-1809
Preprint. Discussion started: 16 April 2026

to the DTS interrogator housed in the climate-controlled DOE ARM facility. The air temperature was -1 to 10 °C at the time of cable installation. The cable was installed at or close to the bottom of the active layer in September 2021 to capture active-layer and near-surface permafrost temperatures, with burial depths of approximately 20 to 40 cm below the ground surface. To minimize disturbance to the ground, the DTS cable was installed manually using shovel and hands (Fig. 1b). A shovel was first pushed into the ground to either a full shovel depth or until reaching the permafrost table, then the shovel was tilted to open a crack in the ground and the cable was inserted and pushed into the bottom of the crack (Fig. 1b); the shovel was removed to close the crack, and the ground surface was pushed from both sides to seal the crack. This process was repeated until the entire cable was installed. At the northeast end, two strands of multimode fiber were spliced together to enable double-ended DTS measurements.

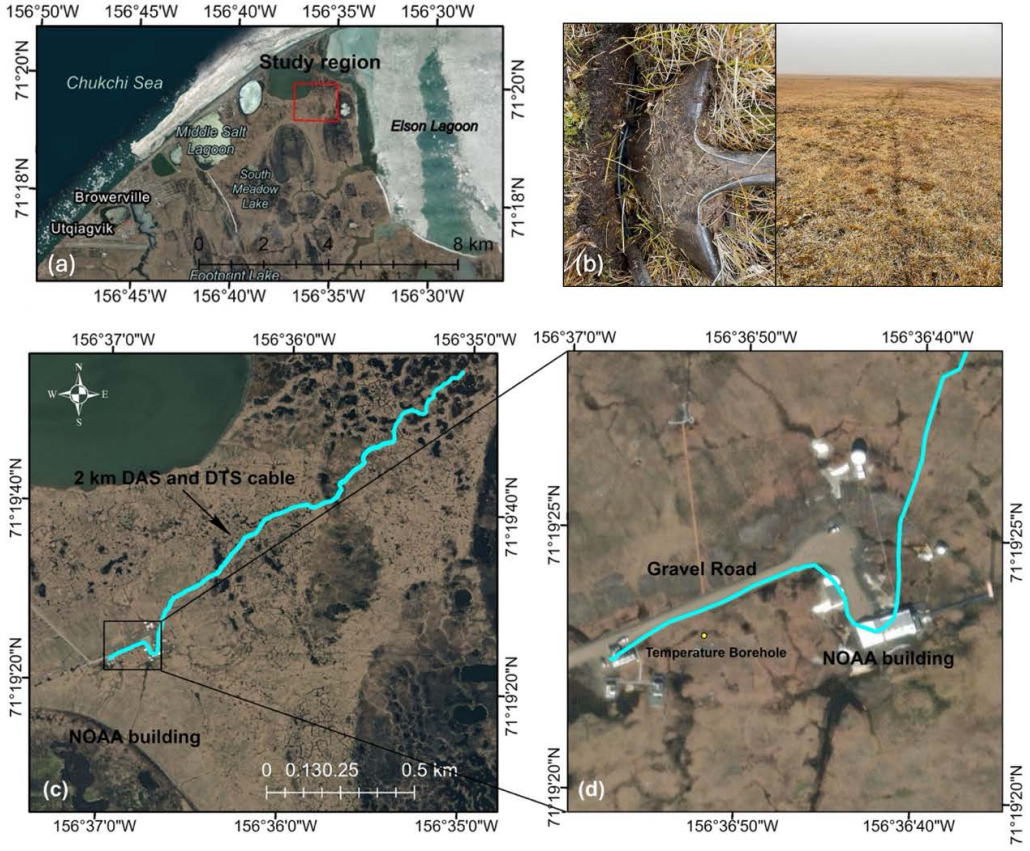

Figure 1. Maps of study region and DTS route in Utqiaġvik, Alaska. Aerial maps are based on ArcGIS (Esri, 2020)

https://doi.org/10.5194/egusphere-2026-1809
Preprint. Discussion started: 16 April 2026

3. Methods

3.1 DTS data processing and calibration

DTS measurements were collected from September 2021 to May 2024 and produced spatially continuous temperature measurements along the full transect. DTS measurements provide temperature estimates at meter-scale spatial resolution along the entire transect and were recorded at 5-min intervals with a nominal temperature accuracy of ±1 °C. Ground temperatures were measured using a Raman-based DTS system, which infers temperature from the ratio of anti-Stokes to Stokes backscattered light along the fiber-optic cable. In the double-ended configuration, both ends of the fiber optic cable are connected to the DTS interrogator, enabling temperature measurements from both directions. This symmetric setup improves measurement accuracy by averaging four readings (two directions and two fibers per direction) for each location and effectively reduces systematic errors caused by fiber attenuation and laser power fluctuations (van de Giesen et al., 2012). Raw DTS measurements were processed to correct for instrument drift and differential signal attenuation along the fiber, with double-ended measurements used to improve temperature accuracy and reduce spatial bias. Calibration followed established multi-point DTS protocols using reference sections maintained at known temperatures and co-located with the fiber, with in situ reference baths and repeated calibration checks applied throughout the monitoring period. Temporal averaging was applied to reduce high-frequency noise while preserving seasonal and interannual variability. Quality control procedures included removal of anomalous readings associated with power interruptions and sensor instability, and periods of missing or unreliable data resulting from system outages were flagged for subsequent reconstruction using the hysteresis-based modeling framework described below. Calibration diagnostics and uncertainty estimates are provided in the Appendix A. Fig. A1 shows the DTS data processing workflow and an example of the processed DTS data. Fig. A2 shows an example of the calibrated temperature profiles with raw DTS data from September 2021 to January 2024.

3.2 Hysteresis model correlating permafrost temperature with air temperature, meteorological factors, and ground surface conditions

To model permafrost temperature dynamics and reconstruct missing DTS observations, we developed a non-linear, multivariate hysteresis-based framework that explicitly represents the asymmetric, lagged relationship between air temperature and ground temperature, while considering meteorological factors and ground surface conditions. Hysteresis is implemented by allowing separate functional responses during freezing and thawing phases, capturing delayed ground responses associated with thermal inertia, latent heat effects, and subsurface heat storage. The model captures the temperature hysteresis of permafrost with the air temperature and considers the effects of wind speed, atmospheric pressure, relative humidity, snow cover, and rainfall precipitation in snow-free season. Meteorological data from the NOAA Barrow Atmospheric Baseline Observatory, collected between 2021 and 2024, were used for this analysis (NOAA, 2024).

Correlation analysis in Fig. 2 shows that relative humidity exhibits a strong positive correlation with air temperature (R = 0.79); atmospheric pressure shows a negative correlation with both air

https://doi.org/10.5194/egusphere-2026-1809
Preprint. Discussion started: 16 April 2026

temperature (R = -0.45) and relative humidity (R = -0.4); and wind speed remains largely independent of the other variables, indicating minimal collinearity. To select the most influencing factors and assess the interdependence of meteorological variables in the hysteresis model, variance inflation factor (VIF), a statistical measure that quantifies the extent of multicollinearity among predictor variables in a regression model, is used. Table B1 presents the collinearity tests. The VIF diagnostics reveal that relative humidity has the least influence on ground temperature thus is removed from the model formulation.

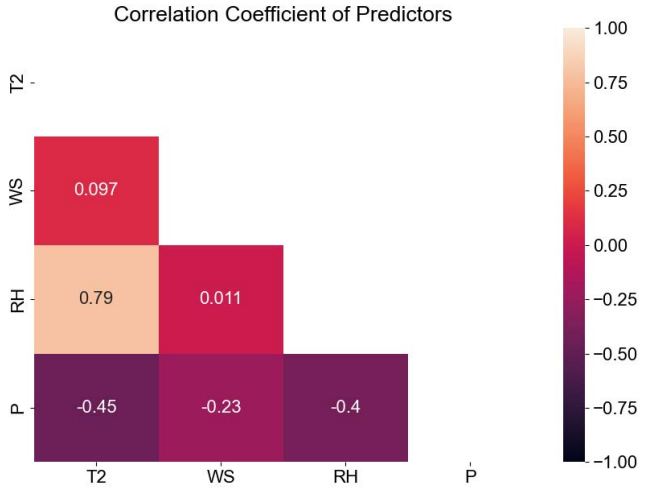

Figure 2. Correlation coefficients between predictors. T2 is air temperature at 2 m above ground, WS is wind speed, RH is relative humidity, P is atmospheric pressure.

The hysteresis model incorporates two distinct equations to account for seasonal variations in ground surface conditions: snow-covered and snow-free seasons. The transition between the two seasons is determined by the albedo of the ground surface (Cox et al., 2017). This seasonal differentiation is critical, as snow cover significantly influences the thermal regime of permafrost by altering heat exchange processes at the ground surface. The basic equations of the hysteresis model of permafrost temperature at the permafrost table for the two seasons are shown in Equations (1) and (2).

Snow-covered season:

$$\boldsymbol{T_d = a_0 + f_1(T_{a(d-H_d)}) + f_2(WS_{d-H_d}) + f_3(P_{d-H_d}) + f_4(SD_d)} \quad (1)$$

Snow-free season:

$$\boldsymbol{T_d = a_0 + f_1(T_{a(d-H_d)}) + f_2(WS_{d-H_d}) + f_3(P_{d-H_d}) + f_5(Pr_d)} \quad (2)$$

where T_d is the permafrost temperature (°C) at date d, d is the date in yyyy-mm-dd format; $T_{a(d-H_d)}$ is the daily air temperature (°C) on the $(d - H_d)$th date due to hysteresis; H_d is the number of days in which daily ground temperature shows hysteresis (or lag) relative to daily air

https://doi.org/10.5194/egusphere-2026-1809
Preprint. Discussion started: 16 April 2026

temperature. WS is wind speed, P is atmospheric pressure, SD is snow depth, Pr is the indicator of precipitation, $\boldsymbol{f_i}(\,)$ are the functions of these variables.

The hysteresis days (H_d) represent the time lag between changes in air temperature and the corresponding response in the permafrost temperature. The longer the hysteresis (larger H_d), the more delayed the system is in reacting to external changes. It reflects the soil thermal diffusivity, depth of measurement, phase changes, and moisture content. H_d is identified with the maximum correlation coefficient between changes in daily permafrost temperature and air temperature (Hou et al., 2015; Zhang et al., 2008). The fitting parameters within each function vary with ground surface conditions. The ground surface condition categories are jointly determined by spatial temperature heterogeneity and visualized ground surface based on ground surface satellite imagery.

Air temperature, wind speed, and atmospheric pressure are incorporated into the hysteresis model with time lags for each location to account for their delayed influence on ground temperature. In contrast, snow cover and precipitation are not modeled with time lags in the hysteresis framework, because their effects on permafrost temperature are assumed to be immediate or cumulative over time, rather than exhibiting a delayed (hysteretic) response like other meteorological variables. Snow cover acts as an insulating layer, reducing heat loss from the ground during winter and delaying thaw in spring, while precipitation alters soil moisture and thermal conductivity, impacting heat transfer processes (Liu et al., 2023). The indicator of precipitation is determined based on intensity and frequency of precipitation, weighted towards more recent data:

$$\boldsymbol{Pr_d} = \sum_{j=0}^{7} \frac{\boldsymbol{I_{d-j}}}{\boldsymbol{j+1}} \tag{3}$$

where $\boldsymbol{I_{d-j}}$ is the $(\boldsymbol{d-j})$th daily precipitation intensity (cm/day), indicating the precipitation event happened $\boldsymbol{j}$ $(j = 0-7)$ days before $\boldsymbol{d}$th day.

Fig. B1 presents an example of the indicator of precipitation $\boldsymbol{Pr}$ in September 2021 compared with precipitation intensity $\boldsymbol{I}$ in Equation (3). The indicator of precipitation reflects the influence of precipitation on soil moisture conditions. The effects of precipitation are typically short-lived, as excess moisture either infiltrates deeper layers, evaporates, or drains away within a few days. By limiting the analysis to the past 7 days, the model focuses on the period during which precipitation has the most significant and measurable influence on near-surface soil conditions. This approach balances the need to account for precipitation's impact while avoiding the inclusion of outdated or irrelevant data that could introduce noise or reduce the model's accuracy.

Based on the VIF diagnostics, the final forms of the hysteresis model of ground temperature at the permafrost table for the two seasons are shown in Equations (4) and (5).

Snow-covered season:

$$\boldsymbol{T_d = a_0 + a_1 T_{a(d-H_d)} + a_2 T_{a(d-H_d)}^{\,2} + a_3 WS_{d-H_d} + a_4 P_{d-H_d} + a_5 \Delta T_d \cdot log\,(SD_d)} \tag{4}$$

Snow-free season:

https://doi.org/10.5194/egusphere-2026-1809
Preprint. Discussion started: 16 April 2026

$$T_d = a_0 + a_1 T_{a(d-H_d)} + a_2 T_{a(d-H_d)}^2 + a_3 WS_{d-H_d} + a_4 P_{d-H_d} + a_5 T_{a(d)} log\,(Pr_d) \quad (5)$$

where $\Delta T_d = T_{a(d)} - T_d$ and is the difference of air temperature and permafrost temperature; $T_{a(d)}$ is the dth daily air temperature that considers hysteresis with ground temperature (°C); SD_d is snow depth of the dth day. The indicator of precipitation Pr is a factor of precipitation data over the last 7 days of the dth day. Pr_d is calculated using Equation (3). $\boldsymbol{a_i}$ (i $= 0 - 5$) are the fitting parameters. The derivations of the parameters in the equations are presented in Appendix B and Figs. B1 and B2. The calculated ground temperature using Equations (4) and (5) across three ground conditions (civil infrastructure area, nonpatterned tundra area, and patterned tundra and ponded surface areas) during October 2022 to September 2023 match well with the DTS measurements (Fig. B3). The calibrated models are then used to reconstruct missing temperature data for the periods of DTS data gaps, producing spatially and temporally continuous ground temperature field. The ranges of the parameters $\boldsymbol{a_i}$ (i $= 0 - 5$) are given in Fig. B4.

In Equations (4) and (5), the effects of snow depth and precipitation on H_d are not considered. Snow layer has an extremely low thermal conductivity (0.1 – 0.5 W/(m K)) and acts as an insulator between the atmosphere and the ground surface (Zhang, 2005). When the air temperature is low and snow cover is thick, the insulating effect of snow cover becomes a stronger factor, preventing the ground from cooling (Vavrus, 2007; Apaloo et al., 2012). In the hysteresis model, the input data are DTS measurements, air temperature, and meteorology data (ARM, 2024; NOAA, 2024, National Weather Services, 2024). The intensity of precipitation refers to the amount of precipitation occurring within a specific time frame and can significantly influence permafrost conditions (Lin et al., 2003). In the hysteresis model, Equation (5) accounts for a 7-day influence period and captures the cumulative effect of precipitation over time (shown in Equation (3)). Precipitation (Pr) is positively correlated with latent heat flux, which enhances net heat loss and contributes to cooling the ground thus influences permafrost temperatures (Lin et al., 2003).

Fig. 3 presents the calculated ground temperature using Equations (4) and (5) across three ground conditions during October 2022 to September 2023. The calculated ground temperatures compare well with the measured ground temperatures using DTS observations. Unlike the thawing process represented by red markers (during May to September 2023) that exhibits rapid temperature shifts due to latent heat absorption, the freezing process represented by black and blue markers is more gradual. This slow thermal adjustment is likely due to the progressive release of latent heat as unfrozen water transitions to ice.

https://doi.org/10.5194/egusphere-2026-1809
Preprint. Discussion started: 16 April 2026

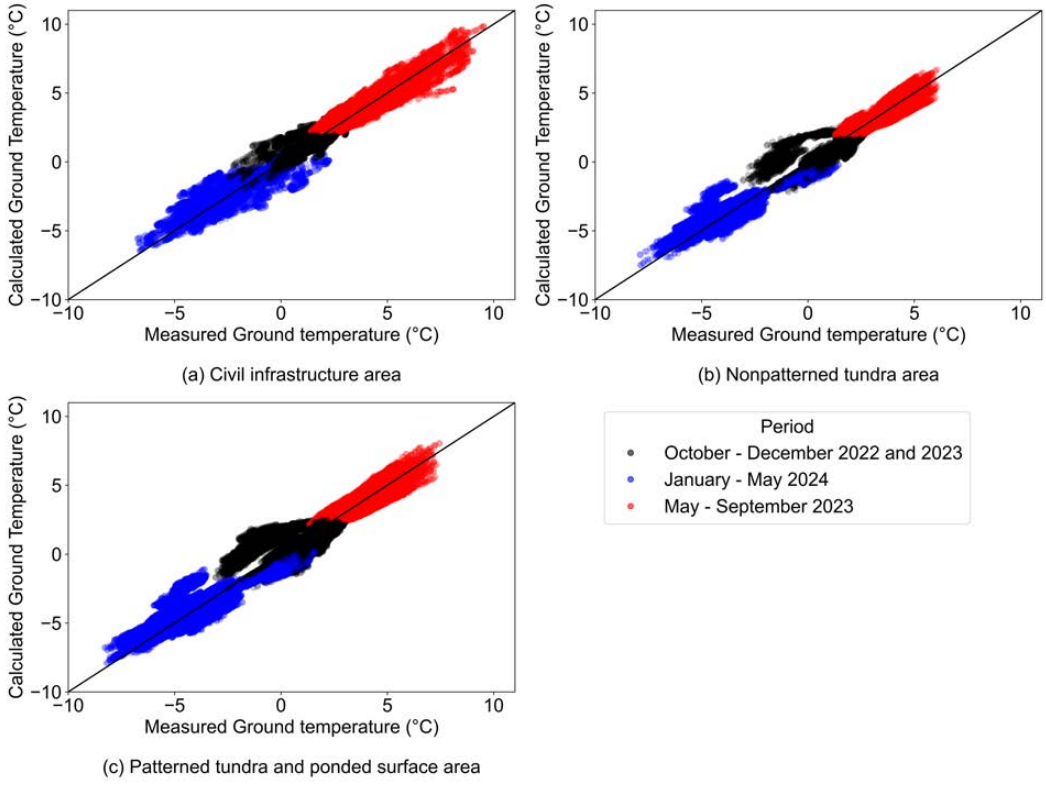

Figure 3. Results of the hysteresis model in different periods: (a) civil infrastructure area; (b) nonpatterned tundra area; (c) patterned tundra and ponded surface areas.

3.3 Permafrost temperature predictions along DTS cable route

Using the averages of five global climate models under the RCP 4.5 and 8.5 climate forcing scenarios, the mean, maximum and minimum annual air temperature predictions for Utqiaġvik, Alaska are derived (Fig 4). The historical and predicted air temperature and meteorology data are collected from the ARM, NOAA and SNAP dataset (ARM, 2024; NOAA, 2024; National Weather Services, 2024; Bieniek, 2019; Lindgren, 2020). Using the air temperatures and the established hysteresis model, we forecast permafrost temperatures through 2075 along the DTS transect. Temperature trajectories are computed independently for each DTS channel, allowing spatial heterogeneity in future projections.

https://doi.org/10.5194/egusphere-2026-1809
Preprint. Discussion started: 16 April 2026

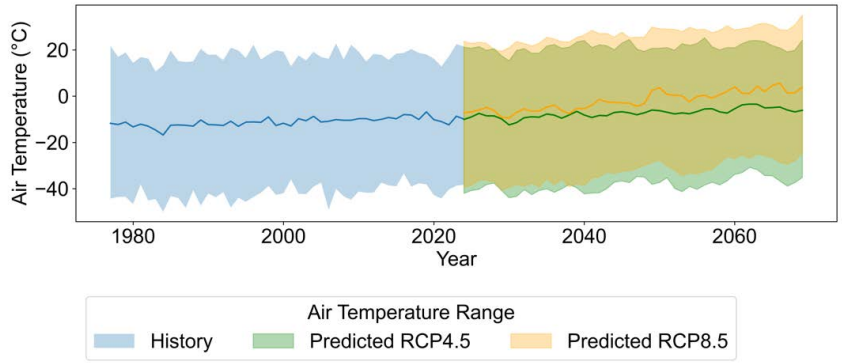

Figure 4. Annual air temperature history data and prediction of Utqiagvik for RCP 4.5 and RCP 8.5 (NOAA, 2024; Lindgren, 2020).

4. Results

4.1 Spatial heterogeneity of permafrost warming

The 2-km DTS cable transect includes three distinct landscapes: the first 0–300 m section traverses civil infrastructure of a gravel road and an office building; the 300–1100 m section crosses undisturbed, non-patterned tundra; and the 1100–2000 m section spans undisturbed, patterned tundra. In all months of DTS data collection, the temperatures in the civil infrastructure zone are consistently higher than those in the tundra. Fig. 5 shows the spatiotemporal variations of the temperature profile at the depth of permafrost table based on available DTS data. The ground temperature ranges from -10 to 10 °C. The localized variability indicates strong impact of micro-environmental conditions, such as cryo-structure, vegetation, snow cover, surface water, and proximity to civil infrastructure on permafrost thermal regime.

The DTS temperate data are validated by borehole temperature measurements (Nicolsky and Wright, 2023). Two boreholes were drilled in August 2022 beside the DTS cable, one is along a road in the infrastructure area, one at approximately 1000 meters away from the infrastructure area. Two thermometers were installed at 0.15 m and 1.5 m depths in each borehole. Fig. 6 shows the air temperature, permafrost temperature measurements obtained from DTS in both the civil infrastructure and tundra areas, and thermometer recordings at depth of 0.15 m. The DTS results closely align with the thermometer readings, validating the reliability of the DTS method.

https://doi.org/10.5194/egusphere-2026-1809
Preprint. Discussion started: 16 April 2026

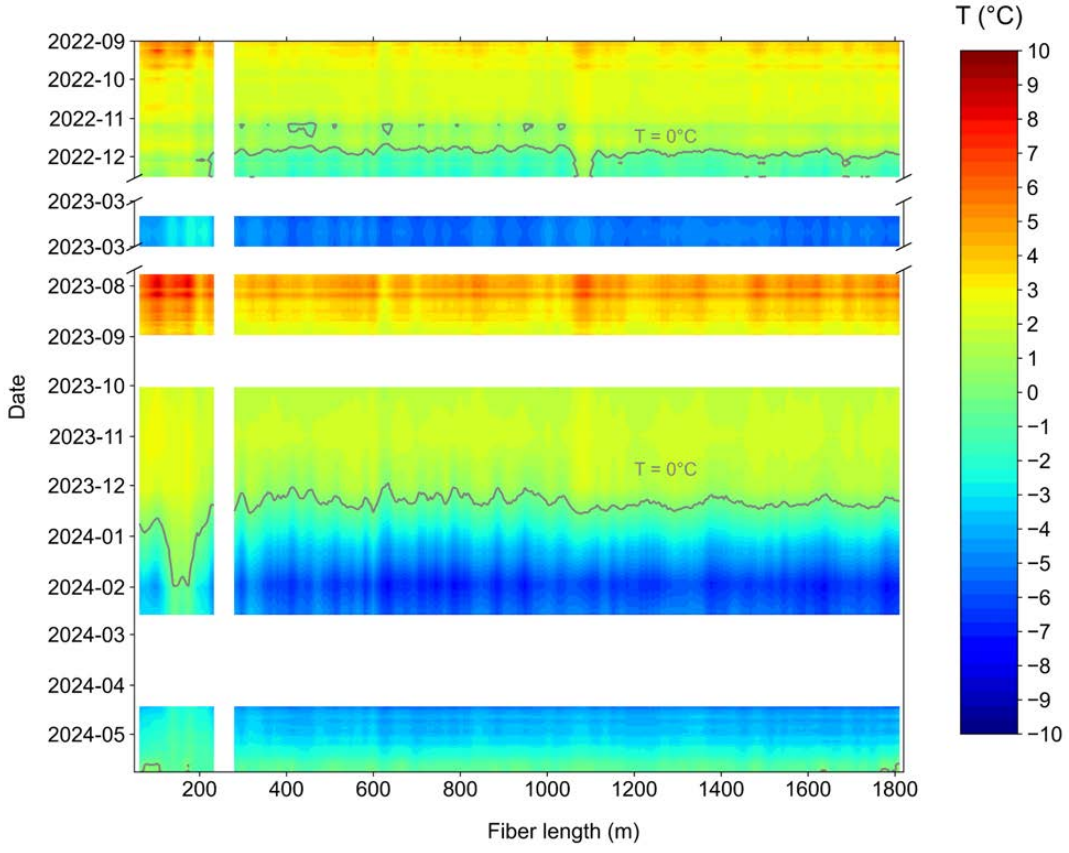

Figure 5. Composed temperature profile based on available DTS data. The vertical blank strip is the section where the DTS cable is attached to a building above ground. Due to power outages, the DTS data in the first year from September 2021 to August 2022 and in other periods represented by horizontal blanks are not shown.

https://doi.org/10.5194/egusphere-2026-1809
Preprint. Discussion started: 16 April 2026

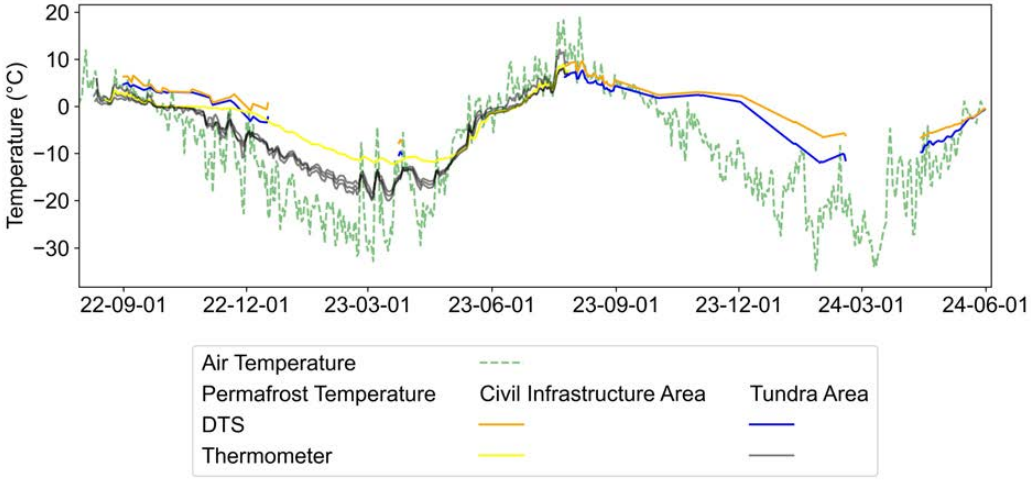

Figure 6. Comparison with air temperature, permafrost temperature measurements obtained from DTS in both the civil infrastructure and tundra areas, and thermometer recordings at depth of 0.15 m. The DTS results closely align with the thermometer readings, validating the reliability of the DTS method.

4.2 Infrastructure-related permafrost warming

As revealed by Fig. 6, ground temperatures at the depth of permafrost table in the civil infrastructure area are approximately 1.4 °C higher than those in the tundra in the entire DTS data collection period, and the difference becomes more pronounced during winter (November to March of the following year), reaching a difference of 3.3°C. This temperature difference highlights the significant thermal influence of civil infrastructure on permafrost, which may have serious implications for the long-term stability of permafrost in developed areas.

The comparison of permafrost and air temperatures in Fig. 7 highlights the temperature dynamics associated with the permafrost's freeze-thaw cycles. This dynamics of permafrost temperature and air temperature is distinctly segmented into two phases: freezing, and thawing. Ground thawing is characterized by faster transition, while ground freezing experiences gradual process due to the asymmetric latent heat exchanged in the phase change. The figure also clearly reveals that ground temperatures in infrastructure area are consistently higher than the those in the tundra throughout the recording period.

https://doi.org/10.5194/egusphere-2026-1809
Preprint. Discussion started: 16 April 2026

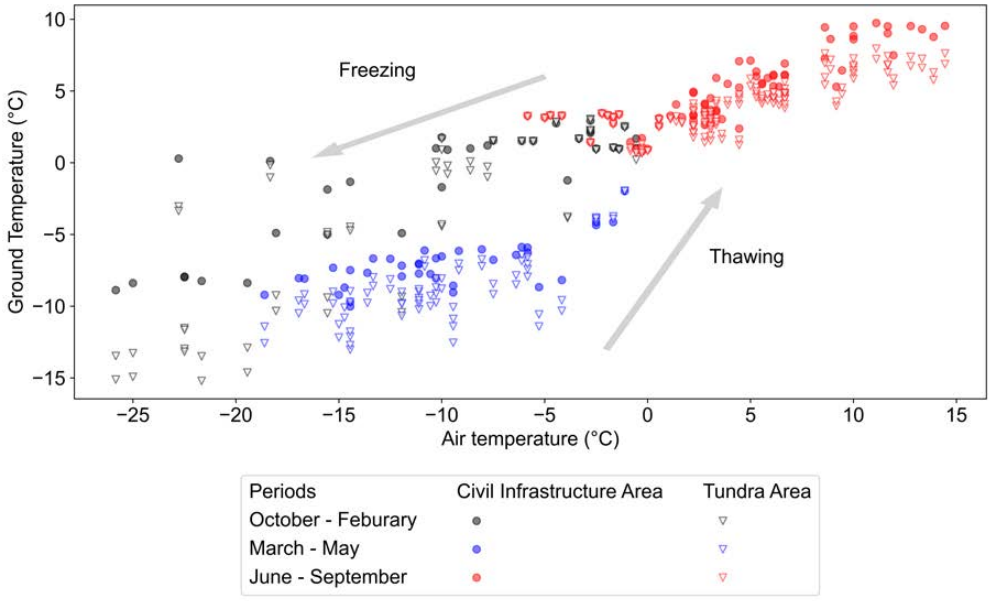

Figure 7. Ground temperature and air temperature comparison from September 2022 to May 2024 in civil infrastructure area and tundra area.

4.3 Meter-scale thermal heterogeneity associated with ice-wedge polygon microtopography

High-resolution DTS measurements reveal pronounced meter-scale variability in near-surface ground temperatures that aligns with ice-wedge polygon microtopography along the transect in both summer and winter seasons as shown in Figs. 8a and 8b, which overlay the DTS-derived temperature profile on ground surface satellite imagery. The blue markers indicate constant lower temperature locations, which tend to align with troughs of ice-wedge polygons, compared with adjacent locations, primarily due to the presence of ice wedges beneath the troughs. This phenomenon is critical for understanding permafrost dynamics in patterned tundra landscapes, as the differential temperature distribution within these polygons can lead to localized thawing and subsidence.

https://doi.org/10.5194/egusphere-2026-1809
Preprint. Discussion started: 16 April 2026

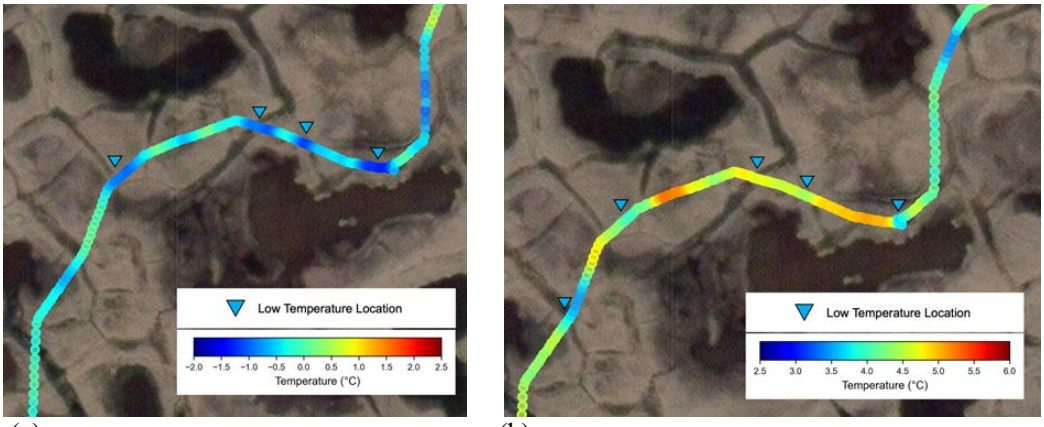

(a) (b)

Figure 8. Ground temperatures in ice-wedge polygon region with distance along fiber 1560 m – 1730 m in December 2022 (a), and July 2023 (b). Aerial maps are based on ArcGIS (Esri, 2020)

Fig. 9 illustrates the variations in ground temperature difference in each area over time relative to the mean ground temperature, $T - T_{mean}$, where T_{mean} is the mean ground temperature of the entire 2 km DTS cable route at the depth of permafrost table. During July to September 2023, the nonpatterned tundra area had the lowest temperatures compared to other areas. Outside of this period, it exhibits similar or even higher temperatures compared to the patterned permafrost and ponded permafrost areas. The patterned tundra and ponded surface areas demonstrate a similar temperature variation pattern, indicating that both experienced similar thermal dynamics throughout the year. This observed behavior suggests that the thermal properties of non-patterned tundra are more sensitive to seasonal fluctuations during the summer months, likely due to reduced surface insulation and increased exposure to atmospheric heat. Civil infrastructure area consistently shows positive deviation from the mean permafrost temperature along the DTS transect.

Together, these observations demonstrate that DTS measurements capture persistent meter-scale heterogeneity in ground temperatures associated with ice-wedge polygon microtopography. The spatial continuity of the DTS dataset allows direct resolution of microtopographic thermal structure along the transect, revealing fine-scale variability that is not accessible using point-based temperature measurements.

https://doi.org/10.5194/egusphere-2026-1809
Preprint. Discussion started: 16 April 2026

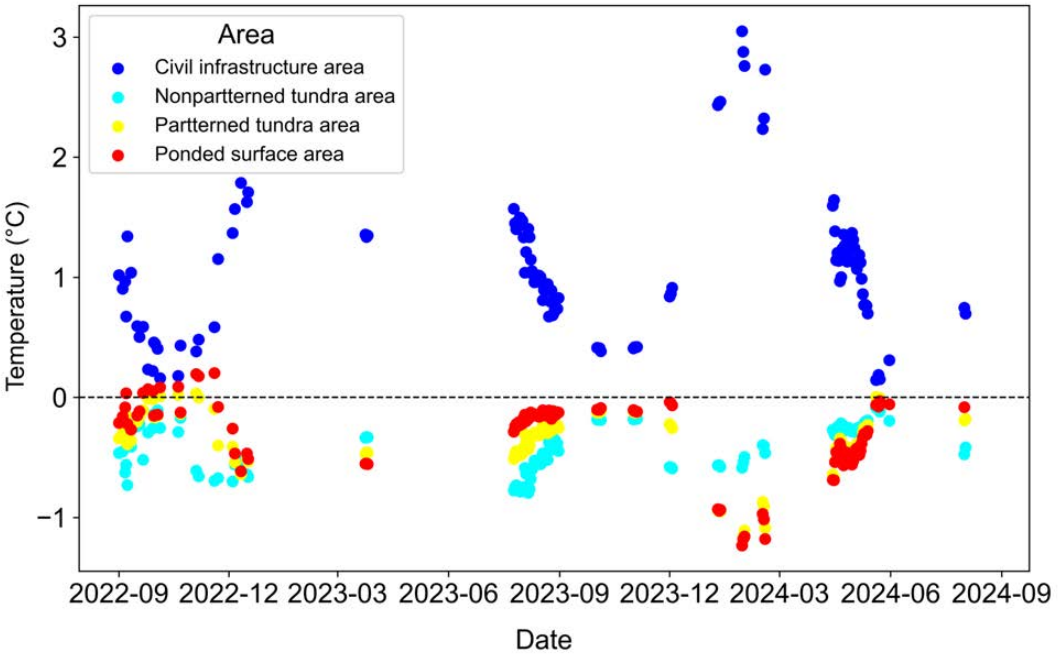

Figure 9. Temporal variations of subsurface temperature relative to the mean subsurface temperature.

4.4 Hysteresis-model reconstruction of missing DTS observations and freeze–thaw dynamics

The multivariate hysteresis model successfully reconstructs missing DTS observations and captures seasonal freeze–thaw behaviors across the transect. Fig. 10 presents a complete temperature profile from September 2021 to May 2024, with data gaps filled by model estimates. A clear pattern emerges in the annual freezing processes: subsurface temperatures dropped below 0°C in October 2021, November 2022, and December 2023, with one month delay of ground freezing in each year. These transitions are closely linked to the local air temperature trends. In the comparatively warmer year (winter of 2022-2023), permafrost freezing occurred later, and the freeze duration was shorter, even though in all three years, air temperatures fell below 0°C starting in October. Fig. 10 shows that reconstructed temperature fields closely match observed DTS measurements during periods of continuous data availability, reproducing both the timing and amplitude of seasonal temperature variations. Model performance is consistent across multiple years and along the full length of the transect. Temporal alignment of freeze onset and thaw progression is preserved. The hysteresis-based reconstruction reproduces spatial patterns of temperature heterogeneity observed in the original DTS measurements. This spatial fidelity is maintained across both tundra and infrastructure-associated segments of the transect. These results demonstrate that the hysteresis model provides a robust framework for reconstructing incomplete DTS time series while retaining key temporal and spatial characteristics of observed permafrost temperatures.

https://doi.org/10.5194/egusphere-2026-1809
Preprint. Discussion started: 16 April 2026

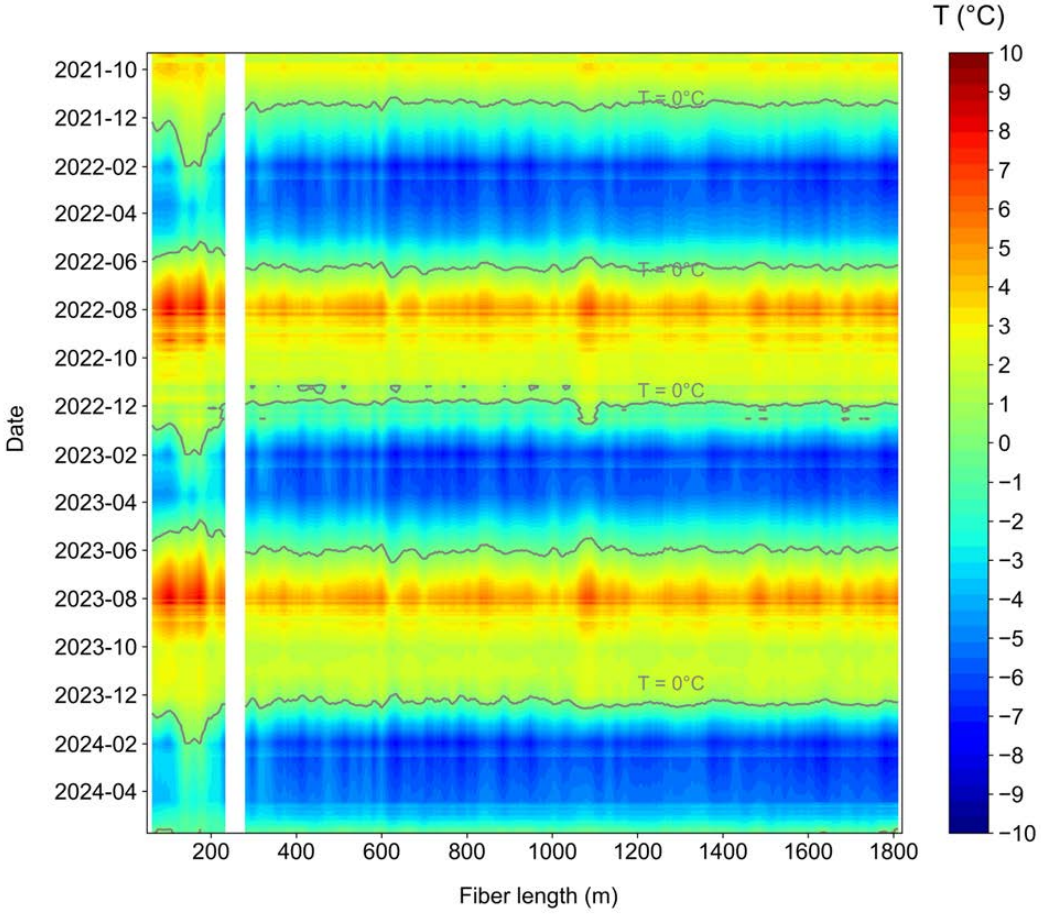

Figure 10. Complete spatiotemporal ground temperature profile at the permafrost table based on DTS measurements and hysteresis model predictions. The vertical blank strip is the section where DTS cable is attached to a building above ground.

4.5 Projected permafrost warming along the DTS transect under future climate scenarios

Using the reconstructed DTS temperature record as a baseline, projected permafrost temperature evolution along the transect indicates continued warming through 2075 under both intermediate- and high-emission climate forcing scenarios (Fig. 11). Projected temperature trajectories show a consistent upward trend across the full transect, with spatial patterns of warming broadly aligned with those observed during the monitoring period. Under the intermediate-emission RCP 4.5 scenario, projected temperatures increase gradually over time, with warming rates varying spatially along the transect (Figs. 11b, 11e). Some segments exhibit stronger warming than others, reflecting persistent lateral thermal heterogeneity evident in the historical DTS observations and enabling assessment of how existing spatial heterogeneity may evolve under future climate forcing. Despite differences in magnitude, warming is observed across all transect segments. Under the high-emission RCP 8.5 scenario, projected warming is more pronounced (Figs. 11c,

https://doi.org/10.5194/egusphere-2026-1809
Preprint. Discussion started: 16 April 2026

11f). The divergence between the two scenarios increases over time, particularly after mid-century. Spatial contrasts in temperature remain evident, with warmer and cooler zones maintaining relative differences throughout the projection period.

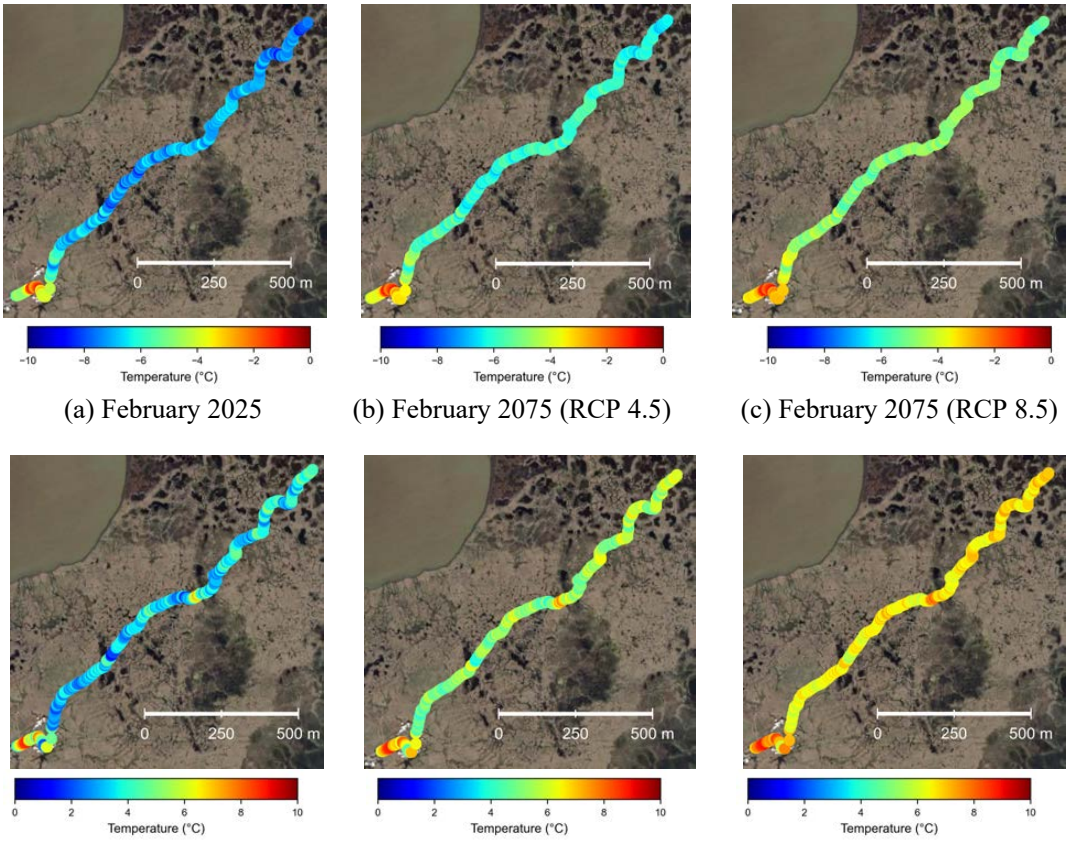

(a) February 2025 (b) February 2075 (RCP 4.5) (c) February 2075 (RCP 8.5)

(d) July 2025 (e) July 2075 (RCP 4.5) (f) July 2075 (RCP 8.5)

Figure 11. Permafrost temperature predictions under RCP 4.5 and RCP 8.5 along the DTS cable route. Aerial maps are based on ArcGIS (Esri, 2020)

5. Discussion

5.1 Spatial heterogeneity as a defining characteristic of near-surface permafrost warming

The DTS observations demonstrate that near-surface permafrost warming is highly heterogeneous at both kilometer and meter scales, even within a single, contiguous tundra landscape. Persistent lateral temperature contrasts observed along the transect indicate that permafrost thermal regimes cannot be adequately represented by spatially sparse point measurements alone. These findings reinforce the growing recognition that permafrost warming

https://doi.org/10.5194/egusphere-2026-1809
Preprint. Discussion started: 16 April 2026

is not spatially uniform, but instead reflects the combined influence of local surface conditions, subsurface properties, and landscape structure (Romanovsky et al., 2010; Biskaborn et al., 2019).

The stability of spatial temperature patterns across multiple years suggests that heterogeneity is a structural feature of the system rather than a transient response to short-term climate variability. Warmer and cooler zones identified in the DTS record remain coherent through seasonal freeze–thaw cycles and interannual fluctuations, implying long-lived controls on subsurface heat transfer. Such persistence has important implications for interpreting borehole records, which may capture site-specific behavior that is not representative of surrounding terrain.

5.2 Thermal impacts of transportation infrastructure on permafrost

The consistently higher subsurface temperatures observed along transportation infrastructure corridors relative to adjacent tundra highlight the strong thermal imprint of linear infrastructure on permafrost. The reduced seasonal temperature amplitude associated with infrastructure-aligned segments indicate sustained modification of subsurface thermal conditions rather than episodic disturbance. These results align with previous observations of infrastructure-related permafrost warming and degradation in Arctic environments (Farquharson et al., 2019; Hjort et al., 2018).

Importantly, the DTS measurements reveal that infrastructure-associated warming extends laterally beyond the immediate footprint of the corridor and persists below the active layer. This suggests that thermal disturbances introduced at the surface can propagate into the underlying permafrost, potentially reducing long-term ground stability. The spatial continuity of the DTS dataset provides direct evidence of how infrastructure modifies permafrost temperature fields over distances that are difficult to capture using discrete monitoring approaches.

5.3 Microtopographic controls on permafrost thermal regimes

At the meter scale, DTS observations resolve distinct thermal signatures associated with ice-wedge polygon microtopography. Systematic temperature differences between polygon centers, rims, and troughs demonstrate that microtopographic position exerts a first-order control on near-surface permafrost temperatures. These contrasts persist through seasonal transitions and extend below the active layer, indicating that microtopography influences subsurface heat storage and transfer rather than only surface energy balance.

The ability to directly observe polygon-scale thermal structure provides new insight into the role of fine-scale landscape features in shaping permafrost response to climate forcing. Such microtopographic variability is likely to influence thaw progression, hydrologic connectivity, and the development of thermokarst features, reinforcing the need to account for small-scale heterogeneity when assessing permafrost vulnerability.

5.4 Value of hysteresis-based reconstruction for long-term DTS analysis

The hysteresis-based reconstruction framework enables continuous analysis of multi-year DTS observations despite data gaps caused by power interruptions and operational constraints. By explicitly accounting for nonlinear freeze–thaw behavior, the model preserves both temporal

https://doi.org/10.5194/egusphere-2026-1809
Preprint. Discussion started: 16 April 2026

dynamics and spatial heterogeneity in reconstructed temperature fields. Agreement with independent borehole measurements demonstrates that the approach retains physical realism while extending the usability of long-term DTS datasets.

The reconstruction results highlight the importance of incorporating thermal memory and seasonal hysteresis when analyzing permafrost temperature records. Approaches that neglect these effects risk misrepresenting transition periods and attenuating spatial contrasts, particularly in heterogeneous landscapes. The demonstrated ability to reconstruct missing data without smoothing lateral structure expands the potential for DTS to support climate-scale permafrost monitoring.

5.5 Implications for projecting permafrost warming along infrastructure corridors

Projections of permafrost temperature evolution along the DTS transect indicate sustained warming through mid-century under both intermediate- and high-emission scenarios. The persistence of spatial temperature contrasts in the projections suggests that existing heterogeneity will continue to shape future permafrost conditions, rather than being homogenized by regional warming. Infrastructure-associated warm zones remain distinct from cooler tundra segments, implying that areas already experiencing elevated temperatures may continue to represent zones of heightened vulnerability

These results underscore the value of using spatially resolved observational records to constrain projections of permafrost warming. By anchoring future trajectories to measured subsurface temperature patterns, the approach provides a pathway for assessing how localized thermal anomalies may evolve under changing climate conditions.

5.6 Limitations and outlook

Several limitations should be considered when interpreting these results. The DTS transect represents a specific environmental and infrastructural setting, and thermal responses may differ in regions with contrasting soil properties, snow regimes, or infrastructure designs. In addition, projections rely on climate forcing scenarios and assumptions that introduce uncertainty, particularly beyond mid-century. While the hysteresis-based reconstruction performs well across observed conditions, its applicability to substantially altered future regimes warrants continued evaluation.

Despite these limitations, this study demonstrates the power of long-term, high-resolution DTS observations for characterizing permafrost thermal dynamics across scales. The combination of continuous spatial monitoring and physically informed modeling provides a framework for advancing permafrost science and improving assessments of infrastructure resilience in a warming Arctic. The 2-km multimode fiber optic cable is expected to remain in the permafrost tundra, providing a unique future environmental monitoring opportunity to other researchers.

https://doi.org/10.5194/egusphere-2026-1809
Preprint. Discussion started: 16 April 2026

6. Conclusions

This study demonstrates the capability of kilometer-scale distributed temperature sensing (DTS) to resolve near-surface permafrost thermal dynamics across heterogeneous Arctic landscapes. Continuous observations at the boundary between the active layer and permafrost reveal pronounced spatial and temporal variability that is not captured by conventional point measurements. Building on these observations, we developed a data-driven hysteresis model that reproduces the delayed and asymmetric response of ground temperature to atmospheric forcing while incorporating key meteorological and surface controls.

The DTS record shows a persistent warming signal associated with civil infrastructure. Throughout the monitoring period from September 2021 to May 2024, permafrost temperatures in infrastructure areas remained consistently higher than those in adjacent tundra, with an average difference of 1.6 °C and winter contrasts reaching 3.6 °C. These results provide direct evidence that infrastructure substantially alters local permafrost thermal regimes and may increase long-term vulnerability to thaw-related instability.

The observations also reveal strong fine-scale heterogeneity in patterned tundra. Ice-wedge polygon troughs consistently remain cooler than adjacent polygon centers, indicating that subsurface ice distribution and microtopography exert first-order controls on ground thermal conditions. This persistence of meter-scale contrasts shows that permafrost warming is not spatially uniform, but is structured by landscape properties that govern heat transfer and storage.

The hysteresis model captures these dynamics and provides a practical framework for reconstructing missing observations and projecting permafrost temperatures under changing climate conditions. Because monitoring interruptions are common in polar environments, this capability substantially extends the value of long-term DTS deployments. More broadly, the framework offers a transferable approach for linking dense observational datasets with predictive analysis across permafrost terrains with varying ground and surface conditions.

Our results further highlight the importance of latent heat effects in governing freeze-thaw behavior. Rapid warming during thaw and slower cooling during freeze reflect the combined influence of phase change, thermal inertia, and environmental forcing. Together, these processes, amplified by infrastructure disturbance and landscape heterogeneity, shape the trajectory of near-surface permafrost change. This study therefore advances both observational and predictive understanding of permafrost thermal dynamics and provides a foundation for improving assessments of Arctic landscape and infrastructure vulnerability in a warming climate.

Appendix A: DTS data processing approach

Raw DTS data were processed through several steps including calibration, drift correction, and moving spatial averages to generate reliable temperature profiles (Fig. A1a). Calibration was performed using reference fiber sections with known, stable temperatures measured by Probe 2 (Fig. A1b). These sections serve as benchmarks to correct systematic errors. Probe 1 represents a probe that was fed through a wall conduit and attached to the outside of the DOE ARM building

https://doi.org/10.5194/egusphere-2026-1809
Preprint. Discussion started: 16 April 2026

to read air temperature (fiber length 45 – 50 m and 3860 – 3865 m), which should be matched by a section of cable attached to the building before it entered the ground. However, based on the recording shown in Fig. A1b, Probe 1 does not have enough stable sections for calibration. Probe 2 corresponds to a section at room temperature attached to the wall behind the interrogator inside the climate-controlled building, the temperature is matched by the sections of cable inside the building at the beginning and end of the optical path. Therefore, only Probe 2 is used for calibration at the two sections along the cable.

DTS data calibration is performed using a Python-based DTS calibration package (des Tombe et al., 2020). A moving special average is added after the calibration. For double-ended measurements, forward and backward measurements are aligned to improve accuracy. The DTS system may experience drift, a gradual shift in measurements over time, which introduces systematic bias. Drift correction is essential for maintaining long-term data accuracy. This is achieved by referencing stable sections of Probes 2 of the fiber optic cable, where temperature variations are assumed to be minimal (Voigt et al., 2011). Temporal changes in permafrost temperature are assessed by calculating temperature gradients over discrete intervals (Pallard et al., 2023).

The double-ended configuration enhances calibration accuracy by reducing errors across the entire fiber length. Fig. A1c illustrates the estimated variances of noise in the Stokes and anti-Stokes measurements and demonstrates that the weighted variance remains consistently low due to the joint use of forward and backward measurements. Fig. A1d presents an example of the calibrated temperature profiles on September 10, 2021, along with a 95% confidence interval. This shows the temperature variation along the fiber length and how calibration significantly reduces noise in the raw data.

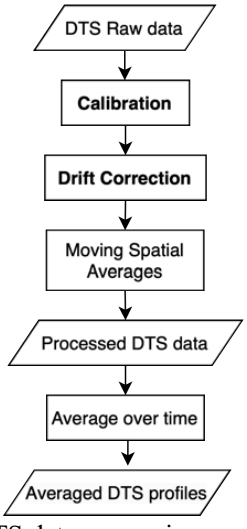

(a) DTS data processing workflow

https://doi.org/10.5194/egusphere-2026-1809
Preprint. Discussion started: 16 April 2026

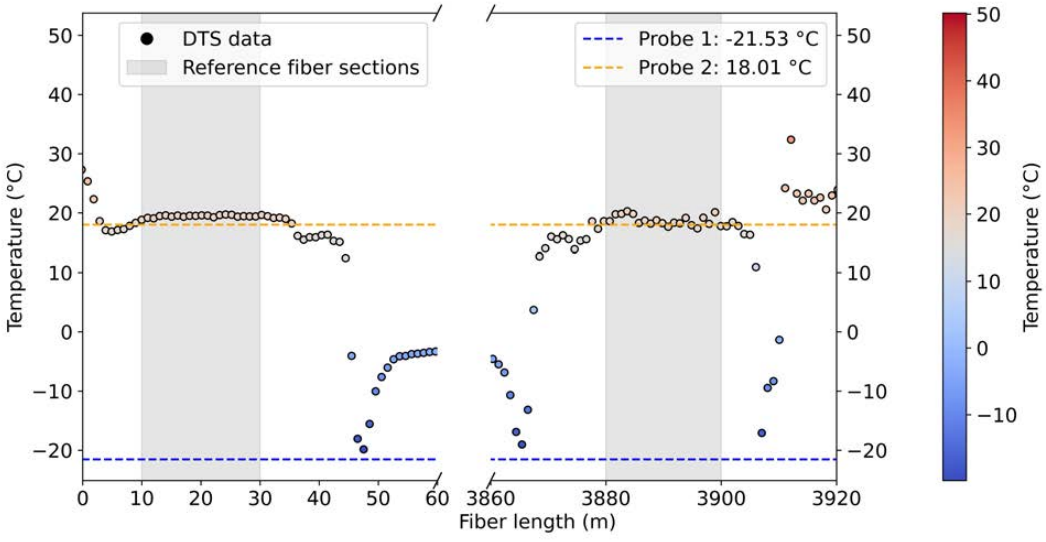

(b) Raw data with reference fiber sections in grey area on December 17th, 2022.

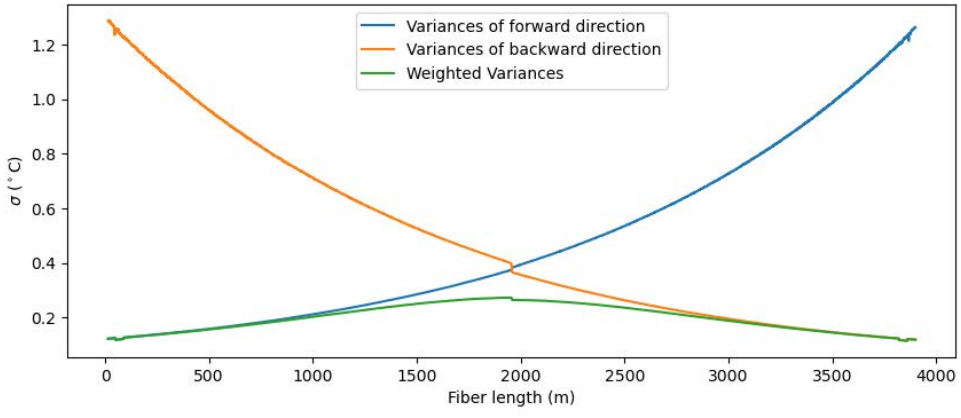

(c) Estimate the variance of the noise in the Stokes and anti-Stokes measurements

https://doi.org/10.5194/egusphere-2026-1809
Preprint. Discussion started: 16 April 2026

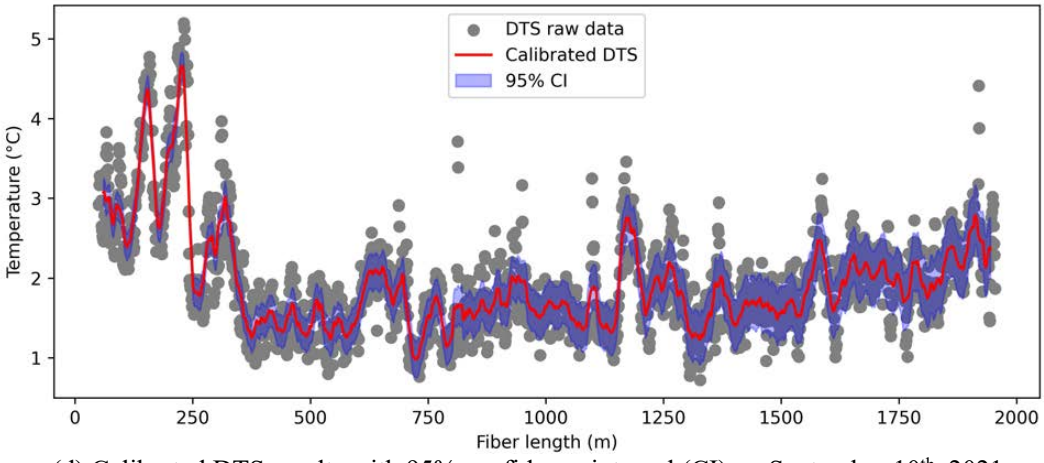

(d) Calibrated DTS results with 95% confidence interval (CI) on September 10th, 2021

Figure A1. DTS data calibration procedure. (a) DTS data processing workflow. (b) Raw data with reference fiber sections in grey area on December 17th, 2022. (c) Estimate the variance of the noise in the Stokes and anti-Stokes measurements. (d) Calibrated DTS results with 95% confidence interval on September 10th, 2021

Figure A2 shows an example of the calibrated temperature profiles with raw DTS data from September 2021 to January 2024.

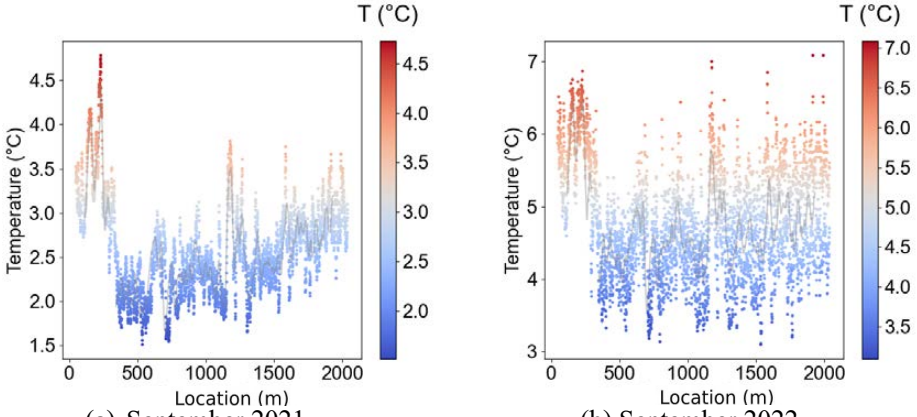

(a) September 2021 (b) September 2022

https://doi.org/10.5194/egusphere-2026-1809
Preprint. Discussion started: 16 April 2026

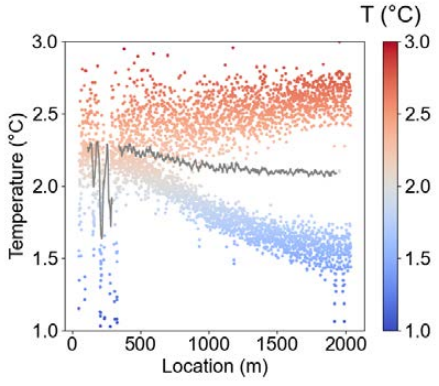

(c) October 2022

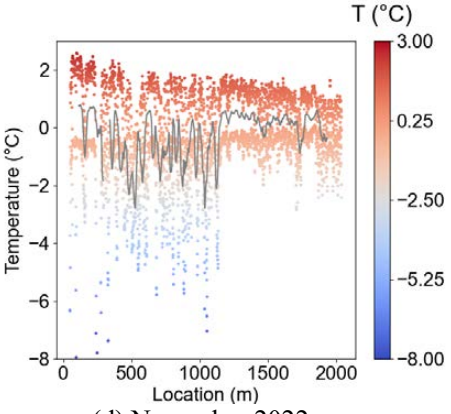

(d) November 2022

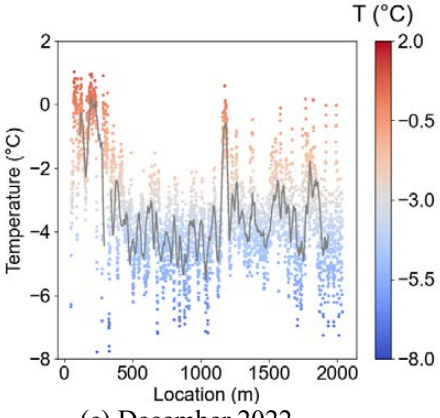

(e) December 2022

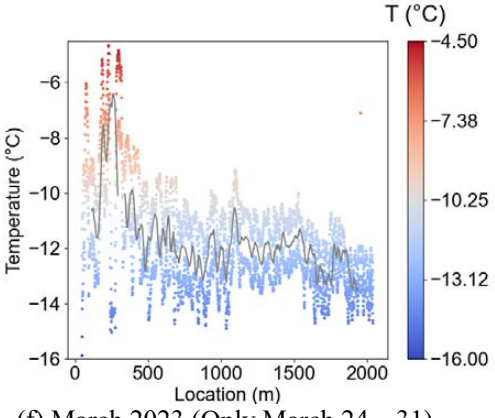

(f) March 2023 (Only March 24 – 31)

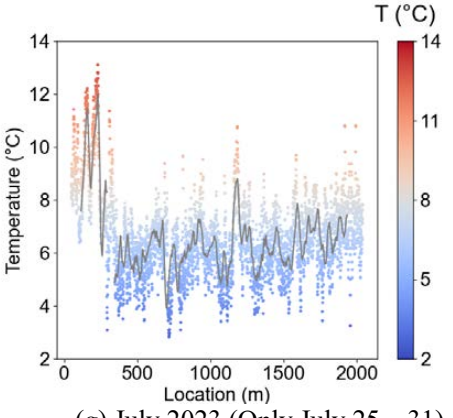

(g) July 2023 (Only July 25 – 31)

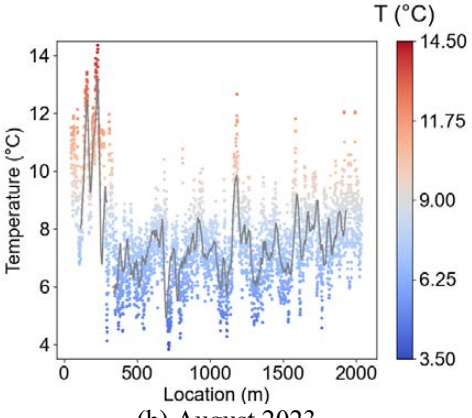

(h) August 2023

https://doi.org/10.5194/egusphere-2026-1809
Preprint. Discussion started: 16 April 2026

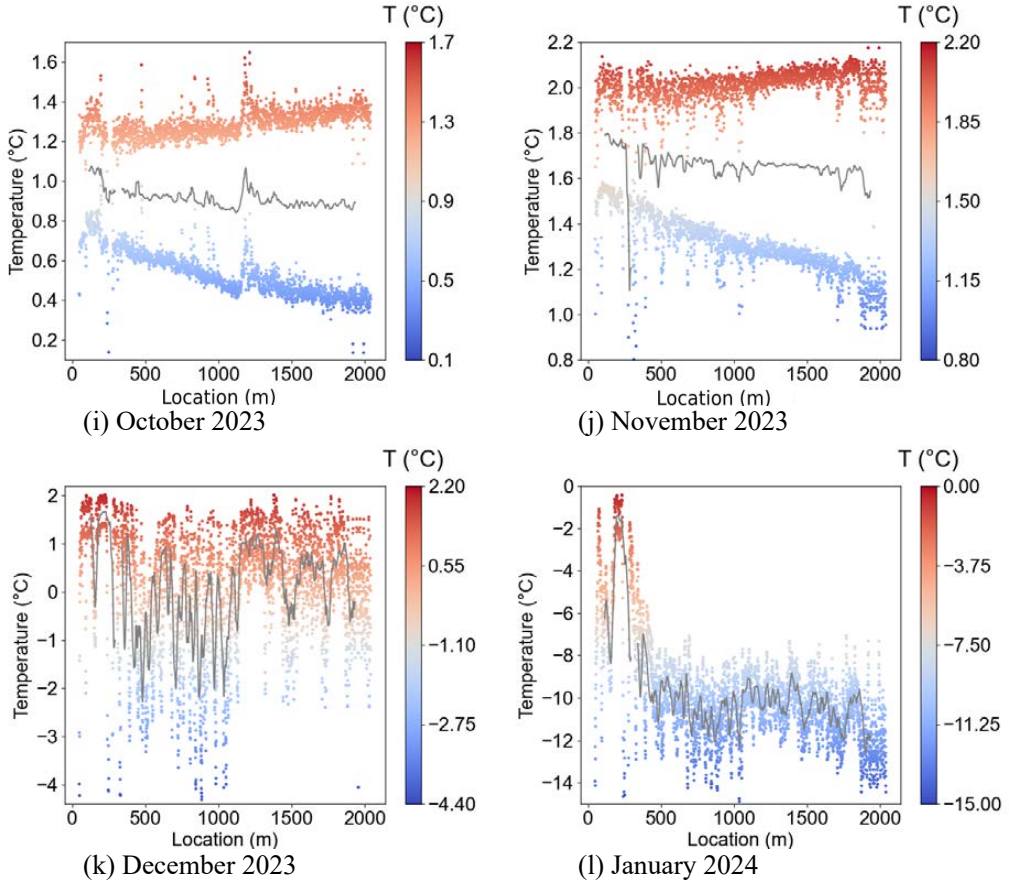

Figure A2. Horizontal 1D temperature profile based on DTS, including near infrastructure and tundra permafrost. In each figure, the line represents the average monthly temperature.

Appendix B: Hysteresis-based model formulation

Table B1 presents collinearity tests using the variance inflation factor (VIF). VIF is used to assess the interdependence of meteorological variables and ensure robust model formulation. The VIF values for the initial set of variables (Round 1) of atmospheric pressure and relative humidity are extremely high (273.38 and 321.38, respectively), indicating significant multicollinearity. In Round 2, relative humidity with the highest VIF is excluded from the model; the updated VIF values decrease substantially, with VIF value of temperature dropping from 5.97 to 1.82 and VIF value of atmospheric pressure decreasing from 273.38 to 6.19, while wind speed VIF value remains relatively stable (5.04 to 5.02). The reduction in VIF values confirms that multicollinearity is effectively mitigated by removing relative humidity. The high VIF value of relative humidity in Round 1 indicates its high correlation with other predictors, particularly air temperature, which

https://doi.org/10.5194/egusphere-2026-1809
Preprint. Discussion started: 16 April 2026

introduces redundancy and instability into the hysteresis model. By excluding relative humidity, the model becomes more stable and simpler, while retaining its predictive capability.

Table B1. Variance Inflation Factor (VIF) of meteorological variables

Variables	VIF in Round 1	VIF in Round 2
Air Temperature	5.97	1.82
Wind Speed	5.04	5.02
Atmospheric Pressure	273.38	6.19
Relative Humidity	321.38	Removed

To partition the cable locations into distinct thermal–hydrological regimes, the K-means clustering algorithm is applied (MacQueen, 1967). K-means seeks to group n observations into k clusters by minimizing the within-cluster sum of squared distances to each cluster's centroid. There are three standardized features considered in the K-means clustering for each location: (1) variation range of temperature offset $T - T_{air}$, (2) mean absolute temperature offset $\overline{|T - T_{air}|}$, and (3) initial ground surface condition categories. To determine the optimal number of clusters, Gaussian mixture models with components k = 1…10 are fitted and evaluated based on their Akaike Information Criterion (AIC) and Bayesian Information Criterion (BIC) values. Both criteria showed an inflection at k = 7. The results of K-means clustering are shown in Fig. B2, the 7 clusters are: completely exposed to air, short sections exposed to air or water, embedded in shallow depth or water, well embedded locations – civil infrastructure and nearby area, embedded in wet area, embedded near ice, well embedded locations – tundra area. Zoomed in sections are shown in Fig. B2, including known cable exposure area (classified as short sections exposed to air or water), cable embedded in ponded surface area (classified as embedded in wet area), ice-wedge polygon center (classified as well embedded locations – tundra area) and trough (embedded near ice). The well embedded locations cluster indicates the cable has no exposure to air, water or large ice body.

Fig. B3 presents the first two features used for the K-means clustering, variation range of temperature offset $T - T_{air}$ and mean absolute temperature offset $\overline{|T - T_{air}|}$. The cluster number is consistent with above. Larger mean absolute temperature offset indicates better isolation between air and permafrost. Well embedded locations of civil infrastructure and nearby area has the highest mean absolute offset $\overline{|T - T_{air}|}$ = 4.4 °C. All the cable sections have mean absolute offset larger than 3.0 °C except for the completely exposed to air cluster, which has the lowest mean absolute offset $\overline{|T - T_{air}|}$ = 2.0 °C. For short sections exposed to air or water, the mean absolute offset is between 3.0 °C – 3.5 °C. Therefore, in the study area, the mean absolute offset of permafrost and air temperature can be used to distinguish cable embedded condition and assist data quality assessment.

https://doi.org/10.5194/egusphere-2026-1809
Preprint. Discussion started: 16 April 2026

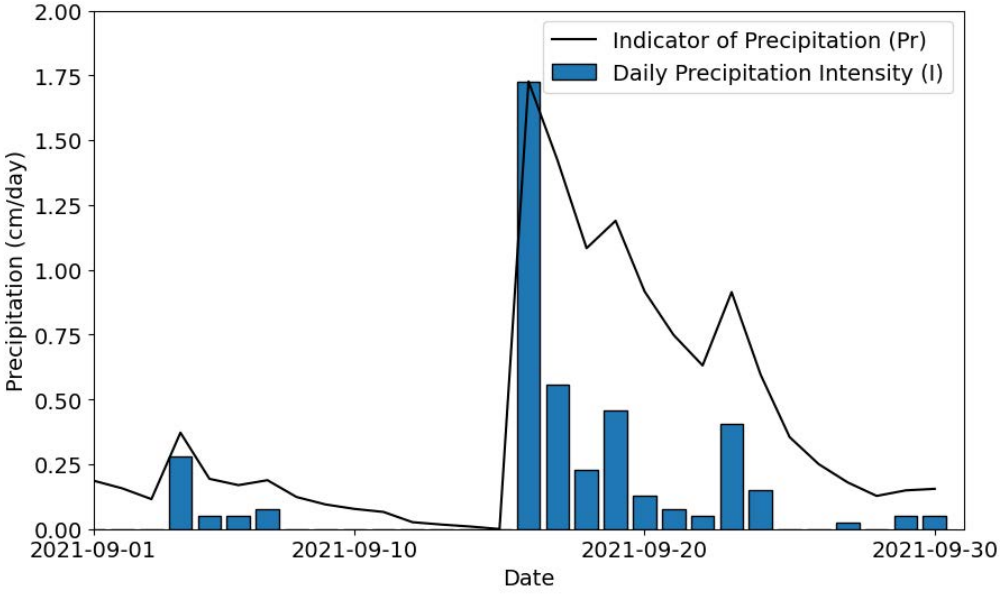

Figure B1. Example of the indicator of precipitation ***Pr*** compared with real precipitation intensity ***I***.

https://doi.org/10.5194/egusphere-2026-1809
Preprint. Discussion started: 16 April 2026

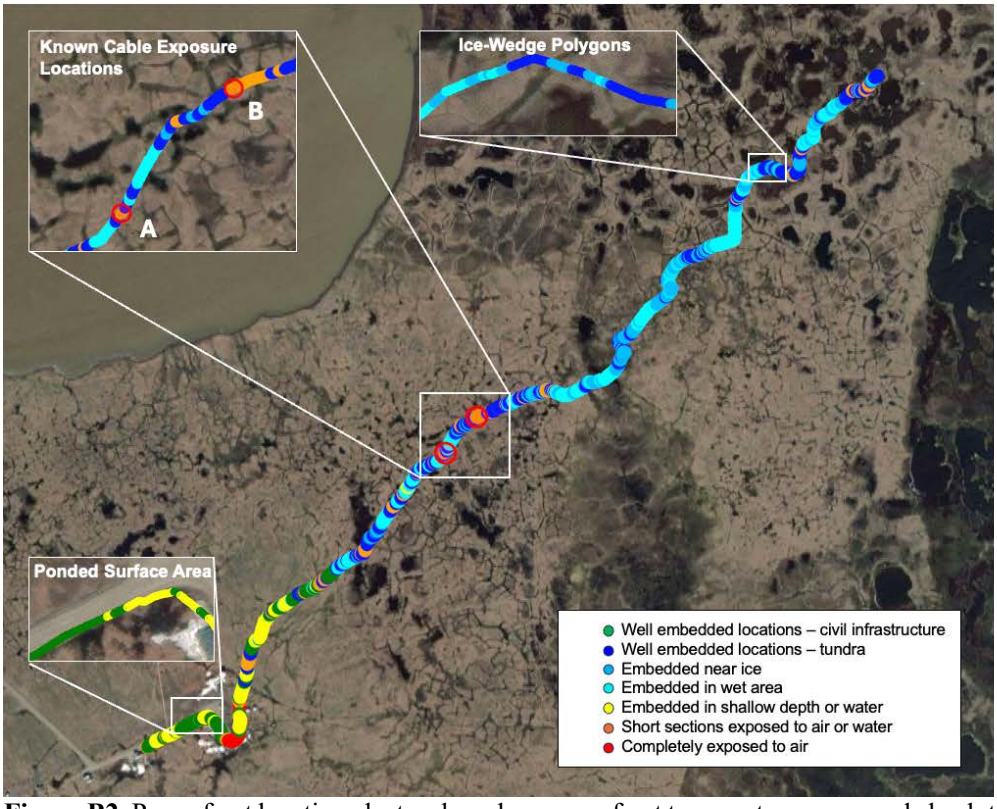

Figure B2. Permafrost location clusters based on permafrost temperature range and absolute offset with air temperature. Aerial maps are based on ArcGIS (Esri, 2020)

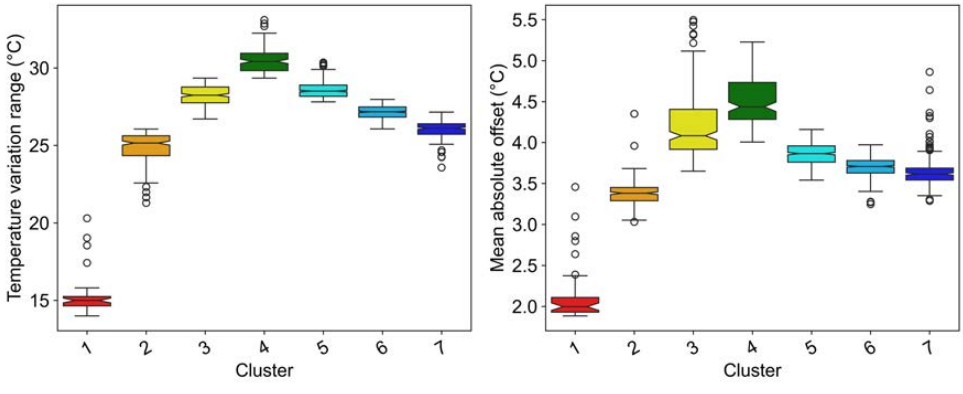

Figure B3. Permafrost temperature clusters temperature variation range and mean absolute offset with air temperature

https://doi.org/10.5194/egusphere-2026-1809
Preprint. Discussion started: 16 April 2026

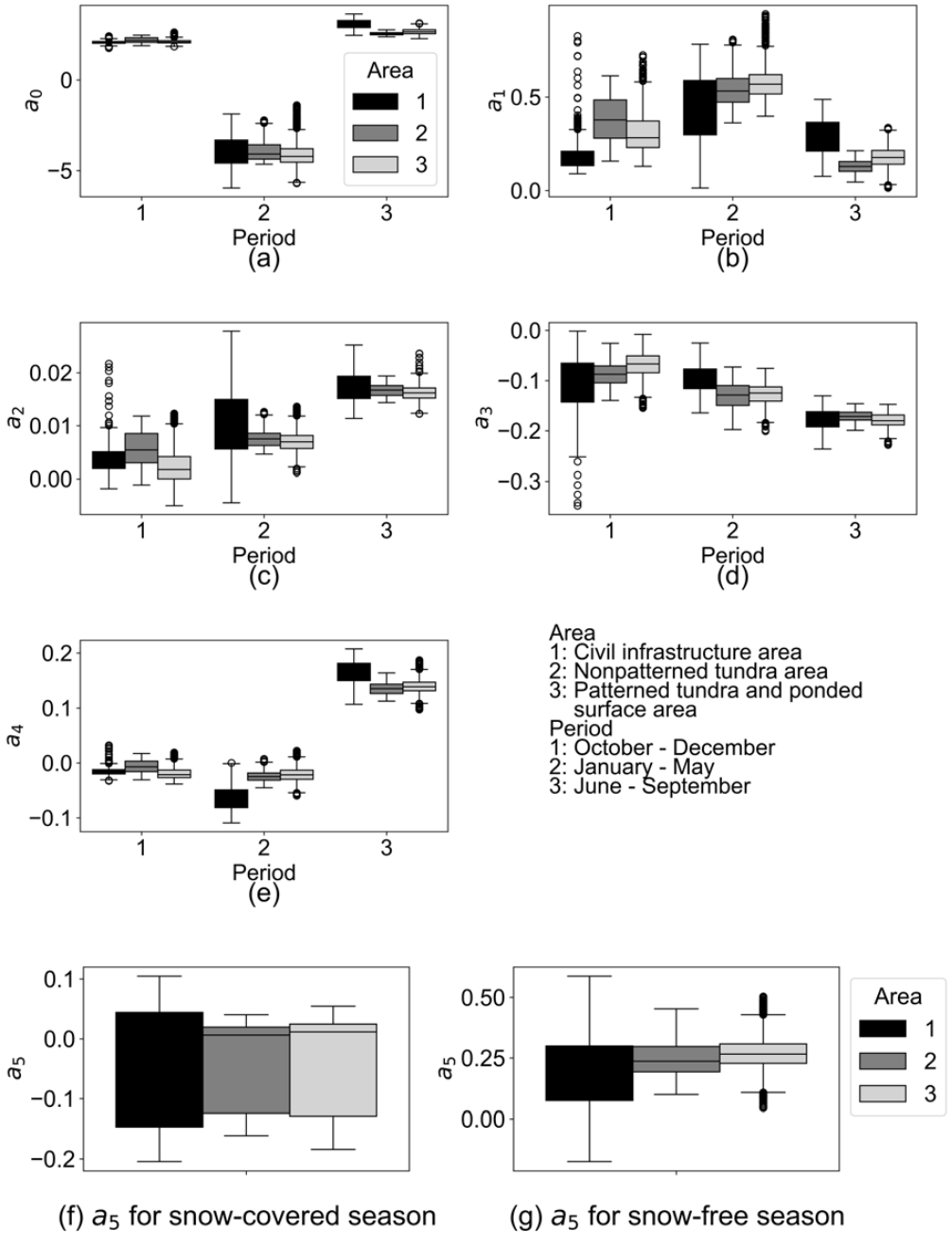

Figure B4. Hysteresis model parameter values. (a) $\boldsymbol{a_0}$; (b) $\boldsymbol{a_1}$; (c) $\boldsymbol{a_2}$; (d) $\boldsymbol{a_3}$; (e) $\boldsymbol{a_4}$; (f) $\boldsymbol{a_5}$ for snow-covered season; (g) $\boldsymbol{a_5}$ for snow-free season

https://doi.org/10.5194/egusphere-2026-1809
Preprint. Discussion started: 16 April 2026

Data availability. The distributed temperature sensing (DTS) data generated during this study, including reconstructed temperature time series, are available on the Arctic Data Center (Ji et al. 2025). Meteorological forcing data used in this study are publicly available from the original data providers. Borehole temperature data used for validation are available on the Arctic Data Center (Nicolsky and Wright 2023). Derived data supporting the findings of this study are included within the paper and its Supplementary Information. The codes used for DTS data processing, hysteresis-based temperature reconstruction, and permafrost temperature projection were developed by the authors and are available on the Arctic Data Center (Ji et al. 2025). The codes rely on standard scientific computing libraries and contain no proprietary dependencies.

Author contributions. X.J., E.R.M., and M.X. developed the original idea. X.J. and M.X. led the manuscript preparation with the contributions from E.R.M. and D.N. E.R. led the instrumentation of DTS system. A.T., E.R.M., and X.J. led the DTS data acquisition and compilation. D.N. led and provided the borehole temperature measurements. All authors participated in DTS development.

Competing interests. The authors declare no competing interests.

Disclaimer. Publisher's note: Copernicus Publications remains neutral with regard to jurisdictional claims made in the text, published maps, institutional affiliations, or any other geographical representation in this paper. The authors bear the ultimate responsibility for providing appropriate place names. Views expressed in the text are those of the authors and do not necessarily reflect the views of the publisher.

Acknowledgements. The Atmospheric Radiation Measurement (ARM) program of the Department of Energy (DOE) supported the DTS data acquisition. National Oceanic and Atmospheric Administration (NOAA) and UIC Science Corporation supported the DTS cable installation. Norlan Roth and Min Liew, doctoral students at Penn State, participated in DTS cable installation.

Financial support. This study was funded by the National Science Foundation through Signals in the Soils (SitS) program under award numbers CMMI-2034363, 2437668, and 2034380.

References

Apaloo, J., Brenning, A. and Bodin, X.: Interactions between seasonal snow cover, ground surface temperature and topography (Andes of Santiago, Chile, 33.5°S). *Permafr. Periglac. Process.* 23, 277–291 (2012).

ARM.: *North Slope of Alaska (NSA) Atmospheric Observatory.* https://www.arm.gov/capabilities/observatories/nsa (2024).

Bieniek, P. A., Walsh, J. E., Thoman, R. L. and Bhatt, U. S.: Using climate divisions to analyze variations and trends in Alaska temperature and precipitation. *J. Clim.* 32, 7031–7056 (2019).

Biskaborn, B. K., Smith, S. L., Noetzli, J., Matthes, H., Vieira, G., Streletskiy, D. A., Schoeneich, P., Romanovsky, V. E., Lewkowicz, A. G., Abramov, A., Allard, M., Boike, J., Cable, W. L., Christiansen, H. H., Delaloye, R., Diekmann, B., Drozdov, D., Etzelmüller, B., Grosse, G., Guglielmin, M., Ingeman-Nielsen, T., Isaksen, K., Ishikawa, M., Johansson, M., Johannsson, H., Joo, A., Kaverin, D., Kholodov, A., Konstantinov, P., Kröger, T., Lambiel, C., Lanckman, J.-P., Luo, D., Malkova, G., Meiklejohn, I., Moskalenko, N., Oliva, M., Phillips, M., Ramos,

https://doi.org/10.5194/egusphere-2026-1809
Preprint. Discussion started: 16 April 2026

M., Sannel, A. B. K., Sergeev, D., Seybold, C., Skryabin, P., Vasiliev, A., Wu, Q., Yoshikawa, K., Zheleznyak, M., and Lantuit, H.: Permafrost is warming at a global scale. *Nat. Commun.* 10, (2019).

Cox, C. J., Stone, R. S., Douglas, D. C., Stanitski, D., Divoky, G. J., Dutton, G. S., Sweeney, C., George, J. C., and Longenecker, D. U.: Drivers and environmental responses to the changing annual snow cycle of northern Alaska. *Bull. Am. Meteorol. Soc.* 98, 2559–2577 (2017).

Cheng, F., Lindsey, N. J., Sobolevskaia, V., Dou, S., Freifeld, B., Wood, T., James, S. R., Wagner, A. M., and Ajo-Franklin, J. B.: Watching the cryosphere thaw: seismic monitoring of permafrost degradation using distributed acoustic sensing during a controlled heating experiment. *Geophys. Res. Lett.* 49, (2022).

Daly, C., Smith, J. and Halbleib, M.: *1981–2010 High-Resolution Temperature and Precipitation Maps for Alaska Final Report.* (PRISM Climate Group, Oregon State University, Corvallis, OR, USA, 2018).

des Tombe, B., Schilperoort, B. and Bakker, M.: Estimation of temperature and associated uncertainty from fiber-optic raman-spectrum distributed temperature sensing. *Sensor* 20, 2235 (2020).

Esri "World Imagery (for Export)" [basemap]. Scale Not Given. "World Imagery (for Export) Basemap." October 15, 2013. https://www.arcgis.com/home/item.html?id=226d23f076da478bba4589e7eae95952. (June 11, 2024).

Farquharson, L. M., Mann, D. H., Grosse, G., Jones, B. M. and Romanovsky, V. E.: Spatial distribution of thermokarst terrain in Arctic Alaska. *Geomorphology* 273, 116–133 (2016).

French, H. M. *The Periglacial Environment.* (John Wiley & Sons, 2017).

Gao, Z., Fan, X. and Bian, L.: An analytical solution to one-dimensional thermal conduction-convection in soil. *Soil Sci.* 168, 99–107 (2003).

Garcia-Ceballos, A. M., Jin, G., Collett, T. S., Merey, S. and Haines, S. S.: Long-term distributed temperature sensing monitoring for near-wellbore gas migration and gas hydrate formation. *SPE J.* 29, 5804–5819 (2024).

Geiger, R., Aron, R. H. and Todhunter, P.: *The Climate Near the Ground.* (Bloomsbury Publishing PLC, 2009).

Goodrich, L. E.: The influence of snow cover on the ground thermal regime. *Can. Geotech. J.* 19, 421–432 (1982).

GTNP Database.: *Global Terrestrial Network for Permafrost.* http://gtnpdatabase.org/boreholes (2024).

Harrington, J. S. and Hayashi, M.: Application of distributed temperature sensing for mountain permafrost mapping. *Permafr. Periglac. Process.* 30, 113–120 (2019).

Hasfurther, V. R. and Burman, R. D.: Soil temperature modeling using air temperature as a driving mechanism. *Trans. ASAE* 17, 0078–0081 (1974).

Hjort, J., Karjalainen, O., Aalto, J., Westermann, S., Romanovsky, V. E., Nelson, F. E., Etzelmüller, B., and Luoto, M.: Degrading permafrost puts Arctic infrastructure at risk by mid-century. *Nat. Commun.* 9, (2018).

Hou, J., Li, Q., Xu, X., Xu, Y. and Zhou, J.: Prediction model for soil temperature by statistical regression of air temperature. *J Zhejiang For. Sci Technol* 35, 55–59 (2015).

Hu, G., Zhao, L., Wu, X., Wu, T., Li, R., Xie, C., Xiao, Y., Pang, Q., Liu, G., Hao, J., Shi, J., and Qiao, Y.: A mathematical investigation of the air-ground temperature relationship in permafrost regions on the Tibetan Plateau. *Geoderma* 306, 244–251 (2017).

https://doi.org/10.5194/egusphere-2026-1809
Preprint. Discussion started: 16 April 2026

Jansson, P.-E.: CoupModel: Model use, calibration, and validation. *Trans. ASABE* 55, 1337–1346 (2012).

Ji, X., Xiao, M., Martin, E., Zhu, T. and Nicolsky, D.: Understand and forecast long-term variations of in-situ geophysical and geomechanical characteristics of degrading permafrost in the Arctic - continuously observed ground temperatures using Distributed Temperature Sensing, Utqiagvik, Alaska, 2021–2024. *NSF Arctic Data Center* https://doi.org/10.18739/A2736M43B (2025).

Jorgenson, M. T., Romanovsky, V. E., Harden, J., Shur, Y., O'Donnell, J., Schuur, E. A. G., Kanevskiy, M., and Marchenko, S.: Resilience and vulnerability of permafrost to climate change. *Can. J. For. Res.* 40, 1219–1236 (2010).

Kang, S., Kim, S., Oh, S. and Lee, D.: Predicting spatial and temporal patterns of soil temperature based on topography, surface cover and air temperature. *For. Ecol. Manag.* 136, 173–184 (2000).

Léger, E., Dafflon, B., Robert, Y., Ulrich, C., Peterson, J. E., Biraud, S. C., Romanovsky, V. E., and Hubbard, S. S.: A distributed temperature profiling method for assessing spatial variability in ground temperatures in a discontinuous permafrost region of Alaska. *The Cryosphere* 13, 2853–2867 (2019).

Lin, X., Smerdon, J. E., England, A. W. and Pollack, H. N.: A model study of the effects of climatic precipitation changes on ground temperatures. *J. Geophys. Res. Atmospheres* 108, (2003).

Lindgren, M.: *Projected Monthly Temperature Products - 10 min CMIP5/AR5.* Scenarios Network for Alaska and Arctic Planning (SNAP). https://catalog.snap.uaf.edu/geonetwork/srv/eng/catalog.search#/metadata/815c6708-b6cf-4a46-b5c8-344851063117 (2020).

Liu, Y., Hansen, B. U., Elberling, B. and Westergaard-Nielsen, A.: Snow depth and the associated offset in ground temperatures in a landscape manipulated with snow-fences. *Geoderma* 438, 116632 (2023).

MacQueen, J.: Some methods for classification and analysis of multivariate observations. In *Proceedings of the Fifth Berkeley Symposium on Mathematical Statistics and Probability*. vol. 1, 281–297 (University of California Press, 1967).

National Oceanic and Atmospheric Administration (NOAA).: *Barrow, Alaska – Meteorology data* https://gml.noaa.gov/obop/brw/met.html (2024).

National Weather Service.: *Alaska Snow Data.* https://www.weather.gov/aprfc/snow_depth (2024).

Nicolsky, D. and Wright, T.: *Understand and forecast long-term variations of in-situ geophysical and geomechanical characteristics of degrading permafrost in the Arctic - continuously observed ground temperatures, 2021-2022*.urn:node:ARCTIC https://doi.org/10.18739/A2C53F305 (2023).

Nicolsky, D. J., Romanovsky, V. E. and Panteleev, G. G.: Estimation of soil thermal properties using in-situ temperature measurements in the active layer and permafrost. *Cold Reg. Sci. Technol.* 55, 120–129 (2009).

Pallard, O., Bense, V. F., Bour, O., Davy, P. and Le Borgne, T.: Inferring subsurface thermal dynamics from distributed temperature sensing: A permafrost application. *The Cryosphere* 17, 321–339 (2023).

Roger, J., Allard, M., Sarrazin, D., L'Hérault, E., Doré, G., and Guimond, A.: Evaluating the use of distributed temperature sensing for permafrost monitoring in Salluit, Nunavik. In

https://doi.org/10.5194/egusphere-2026-1809
Preprint. Discussion started: 16 April 2026

Proceedings of the 68th Canadian Geotechnical Conference and 7th Canadian Permafrost Conference (Québec, Canada, 2015). doi:10.13140/RG.2.1.4273.7365.

Romanovsky, V. E., Smith, S. L. and Christiansen, H. H.: Permafrost thermal state in the polar Northern Hemisphere during the international polar year 2007–2009: a synthesis. *Permafr. Periglac. Process.* 21, 106–116 (2010).

Tourei, A., Ji, X., Rocha dos Santos, G., Czarny, R., Rybakov, S., Wang, Z., Hallissey, M., Martin, E. R., Xiao, M., Zhu, T., Nicolsky, D., and Jensen, A.: Mapping permafrost variability and degradation using seismic surface waves, electrical resistivity, and temperature sensing: a case study in Arctic Alaska. *J. Geophys. Res. Earth Surf.* 129, (2024).

Ukil, A., Braendle, H. and Krippner, P.: Distributed temperature sensing: review of technology and applications. *IEEE Sens. J.* 12, 885–892 (2012).

USGS.: *GAP Alaska 2001 (30 m land cover classification).* https://developers.google.com/earth-engine/datasets/catalog/USGS_GAP_AK_2001 (2001).

van de Giesen, N., Steele-Dunne, S. C., Jansen, J., Hoes, O., Hausner, M. B., Tyler, S. W., and Selker, J. S.: Double-ended calibration of fiber-optic raman spectra distributed temperature sensing data. *Sensors* 12, 5471–5485 (2012).

Vavrus, S.: The role of terrestrial snow cover in the climate system. *Clim. Dyn.* 29, 73–88 (2007).

Voigt, C., Lamprecht, R. E., Marushchak, M. E., Lind, S. E., Novakovskiy, A., Aurela, M., Martikainen, P. J., and Biasi, C.: Warming of subarctic tundra increases emissions of all three important greenhouse gases – carbon dioxide, methane, and nitrous oxide, *Glob. Change Biol.*, 23, 3121–3138, 2017.

Wagner, A. M., Lindsey, N. J., Dou, S., Gelvin, A., Saari, S., Williams, C., Ekblaw, I., Ulrich, C., Borglin, S., Morales, A., and Ajo-Franklin, J.: Permafrost degradation and subsidence observations during a controlled warming experiment. *Sci. Rep.* 8, (2018).

Washburn, A. L.: Classification of patterned ground and review of suggested origins. *Geol. Soc. Am. Bull.* 67, 823 (1956).

Wendler, G., Moore, B. and Galloway, K.: Strong temperature increase and shrinking sea ice in Arctic Alaska. *Open Atmospheric Sci. J.* 8, 7–15 (2014).

Westermann, S., Ingeman-Nielsen, T., Scheer, J., Aalstad, K., Aga, J., Chaudhary, N., Etzelmüller, B., Filhol, S., Kääb, A., Renette, C., Schmidt, L. S., Schuler, T. V., Zweigel, R. B., Martin, L., Morard, S., Ben-Asher, M., Angelopoulos, M., Boike, J., Groenke, B., Miesner, F., Nitzbon, J., Overduin, P., Stuenzi, S. M., and Langer, M.: The CryoGrid community model (version 1.0) – a multi-physics toolbox for climate-driven simulations in the terrestrial cryosphere. *Geosci. Model Dev.* 16, 2607–2647 (2023).

Zhang, T.: Influence of the seasonal snow cover on the ground thermal regime: An overview. *Rev. Geophys.* 43, (2005).

Zhang, Y., Zhang, Z., Yao, F., Feng, X. & Li, Q. Analysis on time lag effect of soil temperature compared to meteorological factors. *Res Agricul Mod.* 29, 468–470 (2008).